Soft-Tissue Imaging in a Human Mummy: Propagation-based Phase-Contrast CT

Jenny Romell, MSc • William Vågberg, MSc • Mikael Romell, MD • Sofia Häggman, PhD • Salima Ikram, PhD • Hans M. Hertz, PhD

From the Department of Applied Physics, Biomedical & X-Ray Physics, KTH Royal Institute of Technology/Albanova University Center, SE-106 91 Stockholm, Sweden (J.R., W.V., H.M.H.); Department of Orthopaedics, Hospital of Varberg, Varberg, Sweden (M.R.); Museum of Mediterranean and Near Eastern Antiquities, Stockholm, Sweden (S.H.); and Department of Sociology, Egyptology and Anthropology, American University in Cairo, Cairo, Egypt (S.I.). Received April 20, 2018; revision requested May 29; final revision received July 26; accepted July 30. **Address correspondence to** J.R. (e-mail: *jenny.romell@biox.kth.se*).

Supported by Swedish Research Council and Wallenberg Foundation.

Conflicts of interest are listed at the end of this article.

Radiology 2018; ▪▪:1–7 • https://doi.org/10.1148/radiol.2018180945 • Content code: CT

Purpose: To evaluate phase-contrast CT as a noninvasive alternative to histology in the study of ancient soft tissue.

Materials and Methods: The imaging was performed between May 8 and June 13, 2017. A mummified human hand from ancient Egypt was imaged in a laboratory phase-contrast CT arrangement with propagation-based imaging. The experimental arrangement for propagation-based imaging included a microfocus x-ray source, a rotation stage for the sample, and an x-ray detector. The mummified hand was imaged in two different modes. First, a CT scan of the whole hand was performed in an overview arrangement. Then, a detailed scan of the tip of the middle finger was performed. With imaging distances tailored for a large magnification and to maximize the phase-contrast signal, the estimated resolution in the final images was 6–9 μm.

Results: The overview CT allowed identification of the tendons of the hand, as well as identification of arteries and nerves in the dehydrated soft tissue. In the detailed phase-contrast setting, virtual histology of the soft tissues of the fingertip could be performed. Blood vessels in the nail bed and the microanatomy of the bone marrow and hypodermis were imaged, and the layers of the skin could be distinguished. Round structures in the adipose tissue were identified as the remains of adipocytes.

Conclusion: Laboratory phase-contrast CT enables imaging of the anatomy and microanatomy of mummified soft tissue with sub-10-μm resolution and may serve as a complement or alternative to the classic invasive histologic methods used in soft-tissue paleopathology.

Online supplemental material is available for this article.

Detailed anatomic assessment of mummies has contributed to a better knowledge of the diseases of ancient times and may improve our understanding of modern diseases (1–5). X-ray radiography and CT have long been the methods of choice for nondestructive studies of both human and animal mummies (6–9). These x-ray methods are based on absorption contrast. Consequently, the primary paleopathologic focus has been on diseases and trauma affecting hard tissues, such as bone and teeth (10,11), but also atheroma and parasitic processes through calcified structures (12,13).

Mummified soft tissues, which are an even richer source of information, are often difficult to analyze and traces of diseases may escape detection (1,11,14). Such tissues can be observed with conventional CT, especially with dual-energy systems, but with low observable resolution due to the weak absorption contrast (15,16). This limits the information that can be extracted from such tissues without employing invasive methods, such as histologic analysis, mass spectrometry, and gas chromatography (14). Because of their invasive and potentially destructive nature, these methods are undesirable or unacceptable for the analysis of many old and fragile specimens.

In our study, we evaluated phase-contrast CT as an alternative noninvasive method for analyzing mummified soft tissue. Whereas conventional CT relies on the absorption of x-rays in the sample, phase-contrast CT instead measures the induced phase shift of the x-rays. X-ray phase contrast typically provides superior imaging of soft-tissue details compared with classic absorption contrast, because the phase shift in such tissues are about three orders of magnitude larger than absorption at x-ray energies (17). This leads to better discrimination between tissues as well as higher observable resolution, provided that a phase-sensitive imaging arrangement is used. Several techniques allow the detection of the phase image—for example, interferometry, analyzer-based imaging, grating-based imaging (18), and propagation-based imaging (19). For high-spatial-resolution laboratory imaging, propagation-based imaging appears to be the superior method (20), demonstrating three-dimensional cellular and subcellular resolution bioimaging for a variety of tissues (eg, zebrafish muscles [21], mouse lungs [22], mouse brain [23], and human coronary arteries [24]). In vivo imaging of mouse lungs by using propagation-based imaging has recently been reported (25).

The main purpose of our study was to evaluate phase-contrast CT as a noninvasive alternative to classic histology in the study of ancient soft tissue. We studied a mummified hand from ancient Egypt in a laboratory phase-contrast CT arrangement by using propagation-based phase-contrast CT.

Summary

Propagation-based phase-contrast CT of a mummified human hand was performed, revealing remains of adipose cells, blood vessels, and nerves in ancient tissue.

Materials and Methods

Mummy Sample

Figure 1a shows the detached mummified human hand that was imaged. The right hand (item inventory identification no. MM 18037), today in the collection of the Museum of Mediterranean and Near Eastern Antiquities (Stockholm, Sweden), was brought to Sweden at the end of the 19th century, along with other mummified body parts and a fragment of mummy cartonnage (papier-mâché case). The cartonnage belonged to an Egyptian man and has been dated to around 400 BCE. Skin and fingernails were well preserved, and the hand was wrapped in linen. The length of the sample was 17.5 cm and the maximum width was approximately 8 cm. The hand was placed upright in a plastic cylinder and was padded with plastic foam to avoid movement during imaging.

Propagation-based Phase-Contrast CT

The tomography arrangement is depicted schematically in Figure 1b and a photograph is shown in Figure E1a (online). The components are a microfocus x-ray source, a rotation stage to place the sample on, and an x-ray camera. Detection of the phase shift is achieved by placing the camera at a larger distance (R_2) from the sample. This allows the x-ray beam to propagate and interfere, providing a translation of the phase variations induced by the sample, to intensity variations that can be imaged by the detector. The detected interference pattern, which is proportional to the second-order derivative of the phase, is seen as fringes at the edges of structures in the sample, given sufficiently spatially coherent illumination. The use of phase shift as imaging modality gives better contrast in, for example, soft tissues, which leads to a higher observable resolution compared with absorption imaging.

The distances between source and sample (R_1) and between sample and detector (R_2) can be tailored to achieve desired cone-beam magnification $M = (R_1 + R_2)/R_1$ and phase contrast, governed by the effective propagation distance $z_{eff} = R_1 R_2/(R_1 + R_2)$. The propagation distance is ideally chosen according to $z_{eff} = 1/(2u^2\lambda)$ for maximum phase contrast at a given spatial frequency (u) and wavelength (λ) (26).

The x-ray source (MetalJet D2; Excillum, Stockholm, Sweden) (27) uses a Ga/In/Sn alloy liquid-metal anode and was operated at 80 kV. The spectrum is shown in Figure E1b (online). Tomographic imaging was realized by rotating the sample in small steps between acquisitions with a URS50BCC rotation stage (Newport, Irvine, Calif). The hand was imaged in two different arrangements: an overview scan of the whole sample and a detailed scan of only the tip of the middle finger. The experiments are summarized in the Table and described further below.

Overview CT of Mummified Hand

First, a CT scan of the whole hand was performed. Because of the relatively large size of the sample, the imaging distances R_1 and R_2 were optimized with respect to field of view, not for maximum phase contrast. The images produced are comparable to those of conventional, absorption-based micro-CT. An overview of the experiment is given in the Table. A large-area charge-coupled device detector was used (see Fig E2a [online] for an illustration of the detector point-spread function). A total of nine tomographic data sets were acquired, covering different parts of the hand (see Fig E3 [online] for a map of the scanning pattern). For each set, 900 projections were acquired over 180°, with an exposure time of 10 seconds per projection. The average dose per scan was estimated to a few hundred milligrays (see Appendix E1 and Figure E4 [online] for details).

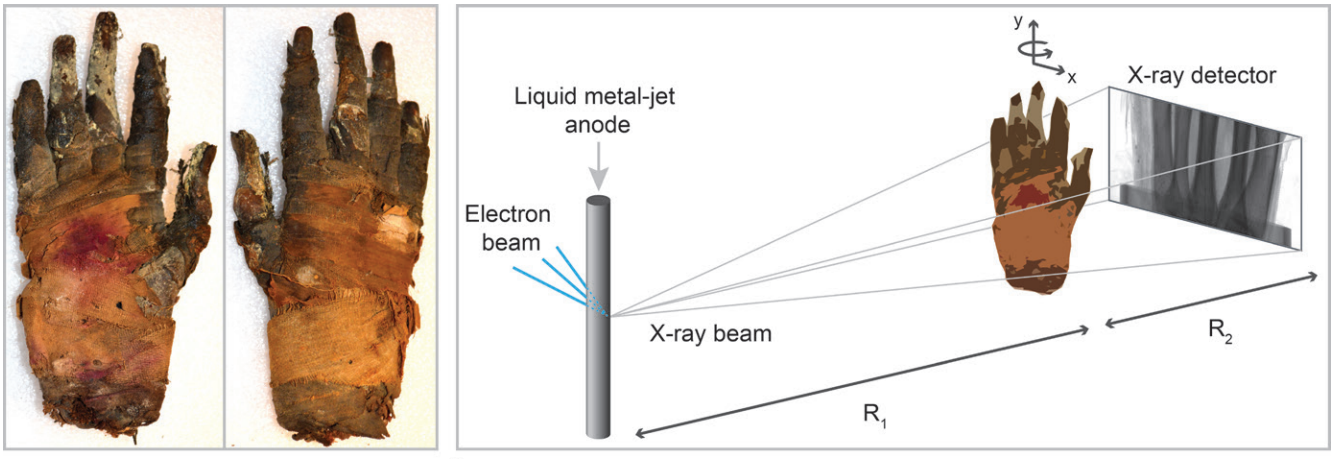

a. b.

Figure 1: Images show propagation-based phase-contrast CT of mummified hand. **(a)** Photograph of human hand that was imaged shows palmar (left) and dorsal (right) views. Hand and parts of fingers are wrapped in linen. Most of skin and all fingernails are well preserved. **(b)** Schematic of experimental arrangement shows microfocus x-ray source, sample placed on rotation stage, and x-ray detector. Photograph of arrangement is shown in Figure E1a (online).

Phase-Contrast CT of Fingertip

For imaging the tip of the middle finger, the requirements on field of view were less stringent. The imaging distances could be optimized for a large magnification, and for a propagation distance maximizing phase contrast of structures with the size of a few micrometers. The propagation distance (z_{eff}) of 315 mm was chosen. For the average wavelength $\lambda = 7.1 \times 10^{-11}$ m, calculated from the measured source spectrum, this propagation distance gives a maximum phase contrast for structures around 3.3 μm (half period). A smaller camera with an effective pixel size of 3.1 μm in the object plane was chosen for this CT scan (see Table for details, and Fig E2b [online] for an illustration of the detector point-spread function). The exposure time per projection was 20 seconds and 1500 projections were acquired over 180°. The average dose was estimated to a few grays. The resolution in the phase-contrast images of the fingertip was estimated to 6–9 μm (half period). Details about the resolution measurement are given in Appendix E1 (online).

Summary of the Experimental Arrangements for the Overview and Phase-Contrast CT Scans of the Mummified Hand

Parameter	Overview CT	Phase-Contrast CT
Area of interest	Whole hand	Fingertip of third finger
X-ray source	MetalJet D2*	MetalJet D2*
Voltage (kV)	80	80
Power (W)	100	70
Electron beam focus (μm)	40 × 10	28 × 7
Emission spot (μm)	Not measured	8 × 10
Source-to-sample distance (mm)	980	480
Sample-to-detector distance (mm)	220	920
Magnification	1.2	2.9
Effective propagation distance (mm)	180	315
Detector	Dual X-Ray FDS Large-Area CCD†	X-Ray FDI-VHR CCD†
Scintillator	CsI‡	Gd_2O_2S:Tb§
Pixel size (μm)	17.3 (14.1)‖	9 (3.1)‖
Point-spread function (μm)	68 (57)‖	24 (8)‖
No. of pixels	5728 × 2254	4008 × 2671
Area (mm)	97 × 38	36 × 24
Exposure time per projection (sec)	10	20
No. of projections	900 over 180°	1500 over 180°
No. of scans	9	1
Total exposure time per scan (h)	2.5	8.3

Note.—CCD = charge-coupled device.

* Manufactured by Excillum (Stockholm, Sweden).

† Manufactured by Photonic Science (East Sussex, England).

‡ Indicates thickness of 100 μm.

§ Indicates thickness of 15 μm.

‖ Data are physical plane values, with sample plane values in parentheses.

Image Preprocessing and Tomographic Reconstruction

All projections were flat-field corrected to account for inhomogeneous x-ray illumination and detector imperfections. For the overview CT scan of the entire hand, projection images of the middle (widest) part were stitched together pairwise to construct projections covering the whole width of the sample. The projections were phase retrieved with the method described by Paganin et al (28), with parameters suitable for retrieving the bone-air interface. The choice of parameters was performed with visual inspection; some remaining phase contrast can be seen around the soft-tissue edges, but this was preferred over a more aggressive phase retrieval that would result in blurring of denser structures, especially the bone. The tomographic reconstruction was performed by using Octopus Reconstruction (version 8.9.3; XRE NV, Gent, Belgium). The computer platform used for reconstructions is described in Appendix E1 (online). Visualization in virtual sections and volume renderings were performed in ImageJ (version 1.51k; National Institutes of Health, Bethesda, Md) and Amira Software (version 6.3.0; Thermo Fisher Scientific, Waltham, Mass), respectively. A volume rendering was performed with cubic interpolation on an image stack binned 6 × 6 × 6 pixels.

Image Analysis and Data Availability

Identification of anatomic features in the reconstructed images of the mummified hand were performed by M.R. (resident physician in orthopedics with 4 years of experience) and J.R. (graduate student with 2 years of experience in tomographic imaging). M.R. and S.I. (professor in Egyptology with more than 20 years of experience) estimated the age at death of the mummified person.

Original data are available from the authors upon request.

Results

Overview CT of Mummified Hand

Figure 2 shows a reconstruction from the overview CT of the hand, comparable to conventional absorption-based micro-CT. In Figure 2a, the bones are depicted in a volume rendering. The distal epiphyses in metacarpals II–V are unfused, as are the proximal epiphysis of metacarpal I and the proximal epiphyses of all phalanges. Sesamoid bones are visible at metacarpals I and V. The metacarpal and phalangeal bone development and the presence of sesamoid bones suggest that the person, presumably a male, was between age 13 and 17 years at his death (29).

In Figure 2b, an axial section through the metacarpals, as indicated by the lowest solid line in the volume rendering of Figure 2a, is shown. At least eight layers of linen can be seen *(A)*, followed by skin *(B)*. In addition to metacarpals I–V, we identify extensor tendons *(C–E)* and flexor tendons *(F–H)*, deep to the distal portion of the carpal ligament *(J)*. Along with the flexor tendons, we find the median nerve *(K)* that branches out distally. Superficial to the carpal ligament, another structure of interest is found *(L)*. Based on its location and branching toward the fourth and fifth finger, this structure may be the ulnar nerve, possibly together with the superficial branch of the ulnar artery. Finally, we identify what is probably the deep branch of the ulnar artery *(M)*, arching across the palm deep to the flexor tendons. Several of the identifications rely on the full three-dimensional data stack, which is shown in Movie 1 (online).

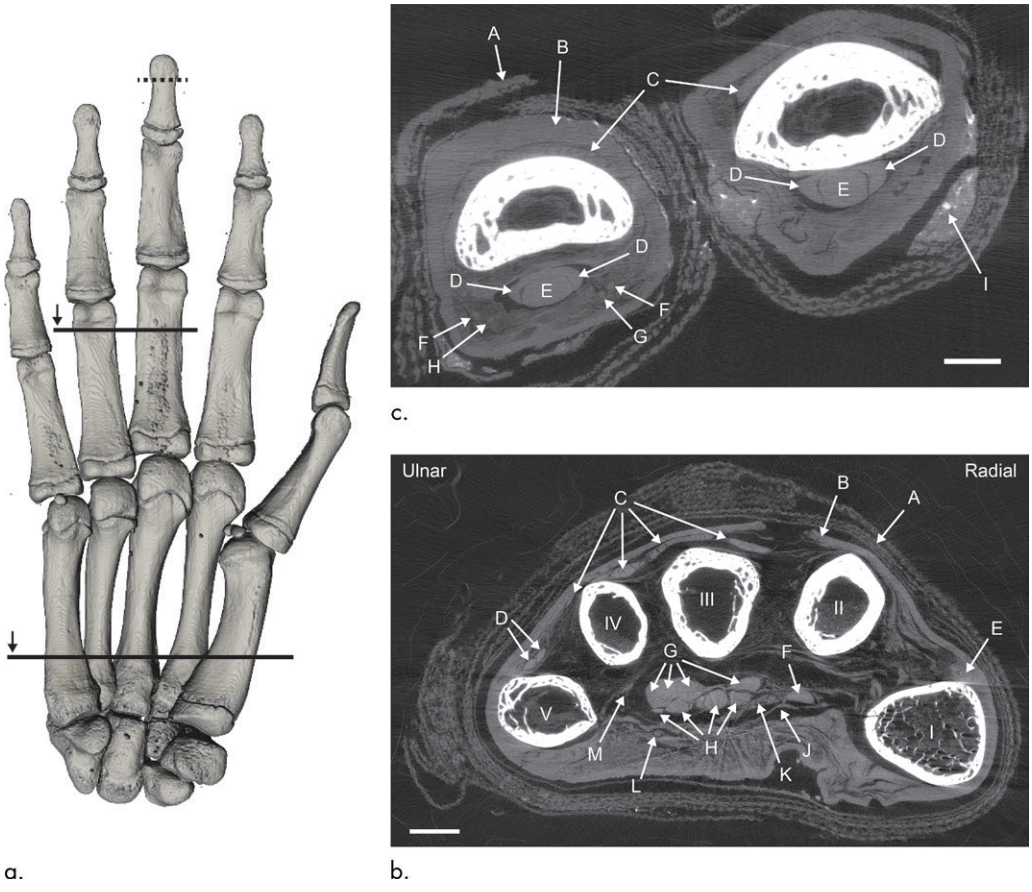

Figure 2: Images show CT of mummified hand. **(a)** Palmar view of volume rendering depicts bones. Physes are visible at bases of all phalanges and at distal ends of metacarpals II–V. Sesamoid bones are seen at metacarpals I and V. Solid lines mark positions of two virtual sections shown to the right. Black arrows indicate viewing direction. Dotted line at tip of middle finger marks location of high-spatial-resolution scan discussed next. **(b)** Axial view of hand. Metacarpals I–V are marked. Arrows indicate linen *(A)*, skin *(B)*, tendons of extensor digitorum communis *(C)*, tendons of extensor digiti minimi *(D)*, tendons of extensor pollicis longus *(E)*, tendons of flexor pollicis longus *(F)*, tendons of flexor digitorum profundus *(G)*, tendons of flexor digitorum superficialis *(H)*, distal portion of carpal ligament *(J)*, median nerve *(K)*, ulnar nerve and/or superficial branch of ulnar artery *(L)*, and possibly deep branch of ulnar artery *(M)*. Scale bar represents 5 mm. **(c)** Axial section through proximal phalanges of third and fourth fingers. Arrows indicate linen *(A)*, skin *(B)*, tendons of extensor digitorum *(C)*, tendons of flexor digitorum superficialis *(D)*, tendons of flexor digitorum profundus *(E)*, proper palmar digital arteries *(F)*, proper palmar digital nerves of median nerve *(G)* and of ulnar nerve *(H)*, and residues from embalming process *(I)*. Scale bar represents 3 mm.

In Figure 2c, an axial section is shown through the proximal phalanges of the third and fourth fingers, as indicated by the upper solid line in Figure 2a. Again, we observe linen *(A)*, skin *(B)*, extensor tendons *(C)*, and superficial and deep flexor tendons *(D, E)*. In the soft tissue, digital arteries *(F)* and digital nerves *(G, H)* can be seen. The high-density structure between the skin and wrapping is embalming material *(I)*, possibly resin.

Phase-Contrast CT of Fingertip

Figure 3a depicts an axial view of the distal phalange of the middle finger, at the location indicated by the dotted line in Figure 2a. The bone *(A)* with trabeculae *(B)* is seen in white. The dry soft tissues surrounding the bone in general are well preserved but shrunken due to their state of dehydration. The nail *(D)* has detached from the nail bed *(C)*, probably during the desiccation process.

With this phase-contrast imaging method, low-contrast features not observed in the overview CT (described previously) can be imaged. For example, in the nail bed, we find regions of rounded structures that are identified as groups of vessels and/or nerves *(F)*. We identify the layers of the skin: epidermis *(G)*, which is loose or missing in some parts, and dermis *(H)*. The hypodermis *(I)*, which in its natural state mainly consists of adipose tissue, lies deeper, and closest to the bone we find the periosteum *(J)*.

Three soft-tissue regions are marked by lines in Figure 3a and are discussed next. The solid line on the side of the bone crosses a group of vessels and possibly nerves. At the dashed line, through the hypodermis, we find round cavities that are 15–25 μm in diameter, shown enlarged in Figure 3b. In Figure 3c, the intensity profile across the cavities is shown. Inside the bone, at the dotted line, there is mainly air, but also traces of bone

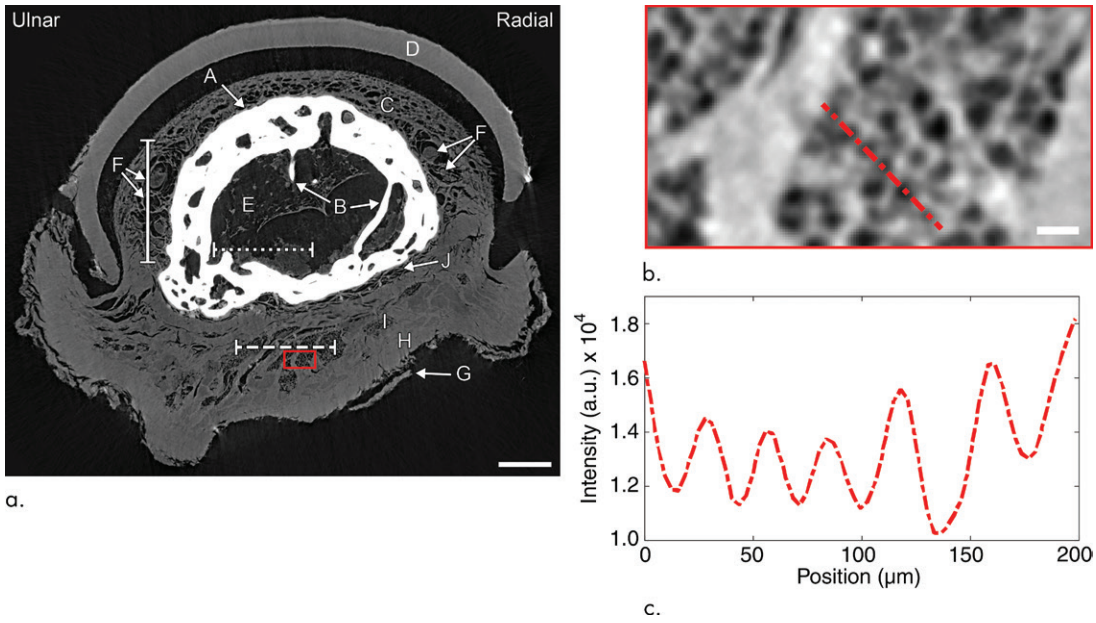

Figure 3: Images show fingertip of mummified hand. **(a)** Axial section through distal phalange of middle finger. Arrows indicate bone *(A)* with trabeculae *(B)*, nail bed *(C)*, nail *(D)*, bone marrow *(E)*, vessels and/or nerves *(F)*, epidermis *(G)*, dermis *(H)*, hypodermis *(I)*, and periosteum *(J)*. Sections at the three lines are shown in Figure 4. Scale bar represents 1 mm. See also Movie 2 (online) for complete set of high-spatial-resolution axial sections of fingertip. **(b)** Detailed view of hypodermis. Scale bar represents 50 μm. **(c)** Line profile shows intensity along dashed red line in **b**.

marrow *(E)*. The soft tissues at these three sections are analyzed in detail next.

Soft-Tissue Analysis

In Figure 4, the microanatomy of the fingertip is shown in three virtual sections. Figure 4a shows a section at the solid line from Figure 3a. Here, one of the larger cavities (*) extends distally, indicating that this hollow structure is a vessel. Neighboring structures extend in similar ways, some hollow (black arrows) and some filled (white arrows). Their spatial arrangement can be clearly seen when browsing through the three-dimensional volume (see Movies 2–4 [online]). These structures are identified as either nerves or blood vessels, some possibly with dried blood still inside.

Figure 4b shows a section through the hypodermis (dashed line in Fig 3a). In the smooth gray region, some air cavities are found (black arrow) as well as denser structures (arrowheads). The exact nature of these is unclear without further analysis. The adipose tissue within the rectangle is shown enlarged in the inset. The small, rounded structures that were observed in Figure 3 appear rounded in this section as well, suggesting that they have an approximately spherical shape. The sizes of the structures are 15–25 μm and their shapes are largely homogeneous. Judging from shape, size and location, these cavities are identified as the remains of adipocytes after dehydration. The streaks between the groups of adipose cells are connective tissue septa (arrows), separating the lobules of adipose tissue.

Figure 4c depicts the bone marrow (dotted line in Fig 3a), which shows similar round structures as the hypodermis. The marked region is shown enlarged in the inset. Here, the cavities enclosed in the tissue are slightly larger (20–40 μm in diameter) and more sparsely distributed. The substances within the bone have agglomerated in different ways; where the cavities were found, the edges are well defined and smooth (white arrow), whereas the mass seen in the lower right part of the figure has a less structured boundary (black arrow). The latter substance is most likely a residue from the mummification process.

Discussion

Mummified remains are a rich source of information about human history, giving insights into lifestyles, death, and diseases of ancient times. Presently, studies of mummified soft tissue are typically performed with classic histologic methods, requiring extraction of material from the sample. Conventional noninvasive imaging methods, such as absorption-based micro-CT, have potential for imaging details down to 10 μm in hard tissue, but the absorption modality does not provide sufficient contrast in soft tissue for observation at high spatial frequencies. MRI and terahertz imaging have recently been proposed for mummies (30,31), but both show much inferior resolution (around 1 mm) and little advantage in soft-tissue contrast for the dry mummified materials. In our study, we investigated propagation-based phase-contrast CT as an alternative to the invasive methods used for examination of mummified soft tissue today. We demonstrate that phase-contrast CT allows nondestructive imaging of the soft-tissue anatomy and microanatomy in mummies, with sub-10 μm resolution, which enables identification of certain cellular-sized features.

The improved image detail described in this article enables nondestructive virtual histology of mummies and has potential importance for paleopathology and related archaeologic studies. In this context, no pathologic features were observed in the

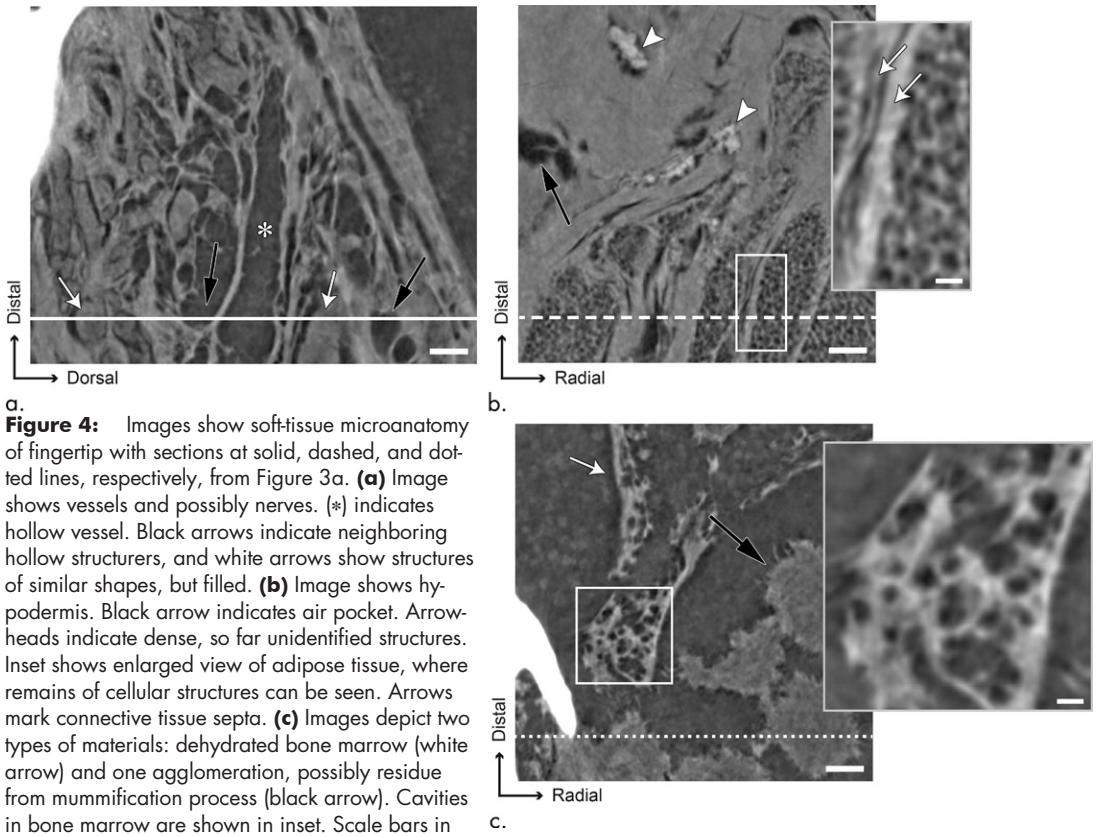

Figure 4: Images show soft-tissue microanatomy of fingertip with sections at solid, dashed, and dotted lines, respectively, from Figure 3a. **(a)** Image shows vessels and possibly nerves. (*) indicates hollow vessel. Black arrows indicate neighboring hollow structurers, and white arrows show structures of similar shapes, but filled. **(b)** Image shows hypodermis. Black arrow indicates air pocket. Arrowheads indicate dense, so far unidentified structures. Inset shows enlarged view of adipose tissue, where remains of cellular structures can be seen. Arrows mark connective tissue septa. **(c)** Images depict two types of materials: dehydrated bone marrow (white arrow) and one agglomeration, possibly residue from mummification process (black arrow). Cavities in bone marrow are shown in inset. Scale bars in main figures represent 200 μm and solid, dashed, and dotted lines mark position of axial section in Figure 3a. In insets, scale bars represent 50 μm.

mummified hand investigated in this article, which is consistent with the young age of the person. In fact, the correspondence between the anatomy and microanatomy determined by the phase-contrast tomography in the mummified tissue and the healthy anatomy and histology as seen in modern textbooks (32,33) is excellent, allowing assignment and identification of tendons, nerves, blood vessels, adipose cells, connective tissue, and different skin layers. The correspondence in soft-tissue details should enable straightforward identification of pathologic features in other samples. Furthermore, phase-contrast CT produces a high-spatial-resolution three-dimensional volume that simplifies and improves the discovery of and differentiation between pathologic and healthy tissue. This gives us the option of searching through the reconstructed images in arbitrary sections or rendered as a complete volume. With current two-dimensional methods for extractive histology, we are limited to viewing the material sectioned in one direction, risking missed features and misinterpreted three-dimensional structures. Finally, the detailed three-dimensional volume map may prove valuable as a positional guide for extraction of samples for biochemical or genetic analysis.

The present mummy phase-contrast CT system is compact, based on a laboratory x-ray source. In principle, synchrotron sources have the brightness to allow similar phase-contrast measurements, as demonstrated on items such as papyrus rolls (34) and amber-embedded insects (35). However, the laboratory format has several advantages in mummy studies. The local nature of the imaging arrangement makes transportation of invaluable and fragile specimens less of an issue. Furthermore, unlimited access to the system provides the possibility to optimize imaging parameters for maximum contrast and resolution. Given the exquisite resolution, which is now limited by x-ray equipment, it appears feasible to detect even smaller soft-tissue structures. Investigations with a laboratory nanofocus x-ray source (36) provide a path for continued studies. Developments of x-ray sources and detectors enable hierarchal x-ray imaging of mummies, with resolutions ranging from millimeters in conventional CT, to micrometers or less in a micro-CT or nano-CT phase-contrast arrangement. This further reduces the need for classic, invasive techniques for analyzing ancient specimens and allows subsequent imaging at different resolutions with the noninvasive modality of choice.

Our study had some limitations. First, for high-spatial-resolution phase-contrast imaging, the field of view was limited. Resolving the interference fringes caused by the phase shift requires an x-ray detector with high spatial resolution, and this often comes at the expense of detection area. Second, phase-contrast imaging requires a microfocus x-ray source to give x-ray illumination with sufficient spatial coherence to show interference. Such sources typically have a low flux because of the small emission spot, and the exposure times using other micro-CT systems than the one described in our study may therefore be much longer. Such long exposure times, in combination with limited field of view and radiation dose, are the main obstacles in

adaptation to live human imaging at this resolution. Finally, the mummified hand imaged in our study showed only healthy tissue. Mummified samples with known pathologies should also be imaged in a high-spatial-resolution phase-contrast CT arrangement to thoroughly evaluate the paleopathologic impact these results might have.

In conclusion, our study shows that laboratory phase-contrast CT enables imaging of the anatomy and microanatomy of mummies with excellent spatial resolution, allowing detection of certain cellular-sized details in the soft tissues of the hand. This opens up the possibility for virtual histology of ancient soft tissue, further reducing the need for classic invasive techniques in the field of paleopathology.

Acknowledgments: The authors thank Inger Jonsson, BSc, for preparing the sample for imaging; Ilian Häggmark, MSc, and Jakob Larsson, MSc, for technical assistance; and Stellenbosch Institutute for Advanced Studies for providing the multidisciplinary environment where this study was inititiated. For discussions on the microanatomy of the fingertip, the authors gratefully acknowledge Professor Laszlo Szekely, PhD (Department of Medicine, Karolinska Institute, Stockholm, Sweden, with 34 years of experience in pathohistology).

Author contributions: Guarantors of integrity of entire study, J.R., H.M.H.; study concepts/study design or data acquisition or data analysis/interpretation, all authors; manuscript drafting or manuscript revision for important intellectual content, all authors; approval of final version of submitted manuscript, all authors; agrees to ensure any questions related to the work are appropriately resolved, all authors; literature research, all authors; experimental studies, J.R., W.V., H.M.H.; and manuscript editing, J.R., W.V., S.H., S.I., H.M.H.

Disclosures of Conflicts of Interest: **J.R.** disclosed no relevant relationships. **W.V.** disclosed no relevant relationships. **M.R.** disclosed no relevant relationships. **S.H.** Activities related to the present article: disclosed no relevant relationships. Activities not related to the present article: is employed by the Museum of Mediterranean and Near Eastern Antiquities. Other relationships: disclosed no relevant relationships. **S.I.** disclosed no relevant relationships. **H.M.H.** Activities related to the present article: disclosed no relevant relationships. Activities not related to the present article: was a board member of and holds stock/stock options in Excillum. Other relationships: disclosed no relevant relationships.

References

1. Aufderheide AC. Progress in soft tissue paleopathology. JAMA 2000;284(20):2571–2573.
2. Bosch X. Look to the bones for clues to human disease. Lancet 2000;355(9211):1248.
3. Prates C, Sousa S, Oliveira C, Ikram S. Prostate metastatic bone cancer in an Egyptian Ptolemaic mummy, a proposed radiological diagnosis. Int J Paleopathol 2011;1(2):98–103.
4. Prates C, Oliveira C, Sousa S, Ikram S. A kidney's ingenious path to trimillennar preservation: renal tuberculosis in an Egyptian mummy? Int J Paleopathol 2015;11:7–11.
5. Aufderheide AC, Rodríguez-Martín C. The Cambridge encyclopedia of human paleopathology. Cambridge, England: Cambridge University Press, 2011.
6. König W. 14 Photographien mit Röntgen-Strahlen: Aufgenommen im Physikalischen Verein zu Frankfurt a. M. Leipzig, Germany: Barth, 1896.
7. Harwood-Nash DC. Computed tomography of ancient Egyptian mummies. J Comput Assist Tomogr 1979;3(6):768–773.
8. McKnight LM, Atherton-Woolham SD, Adams JE. Imaging of ancient Egyptian animal mummies. RadioGraphics 2015;35(7):2108–2120.
9. Murphy WA Jr, Nedden Dz Dz, Gostner P, Knapp R, Recheis W, Seidler H. The iceman: discovery and imaging. Radiology 2003;226(3):614–629.
10. Rühli FJ, Kuhn G, Evison R, Müller R, Schultz M. Diagnostic value of micro-CT in comparison with histology in the qualitative assessment of historical human skull bone pathologies. Am J Phys Anthropol 2007;133(4):1099–1111.
11. Lynnerup N. Mummies. Am J Phys Anthropol 2007;(Suppl 45):162–190.
12. Thompson RC, Allam AH, Lombardi GP, et al. Atherosclerosis across 4000 years of human history: the Horus study of four ancient populations. Lancet 2013;381(9873):1211–1222.
13. Brothwell D, Sandison AT. Diseases in antiquity: a survey of the diseases, injuries and surgery of early populations. Springfield, Ill: Thomas, 1967.
14. Aufderheide AC. The scientific study of mummies. Cambridge, England: Cambridge University Press, 2011.
15. Wanek J, Székely G, Rühli F. X-ray absorption-based imaging and its limitations in the differentiation of ancient mummified tissue. Skeletal Radiol 2011;40(5):595–601.
16. Bewes JM, Morphett A, Pate FD, et al. Imaging ancient and mummified specimens: dual-energy CT with effective atomic number imaging of two ancient Egyptian cat mummies. J Archaeol Sci Rep 2016;8:173–177.
17. Bravin A, Coan P, Suortti P. X-ray phase-contrast imaging: from pre-clinical applications towards clinics. Phys Med Biol 2013;58(1):R1–R35.
18. Pfeiffer F, Weitkamp T, Bunk O, David C. Phase retrieval and differential phase-contrast imaging with low-brilliance X-ray sources. Nat Phys 2006;2(4):258–261.
19. Wilkins SW, Gureyev TE, Gao DC, Pogany A, Stevenson AW. Phase-contrast imaging using polychromatic hard X-rays. Nature 1996;384(6607):335–338.
20. Zhou T, Lundström U, Thüring T, et al. Comparison of two x-ray phase-contrast imaging methods with a microfocus source. Opt Express 2013;21(25):30183–30195.
21. Vågberg W, Larsson DH, Li M, Arner A, Hertz HM. X-ray phase-contrast tomography for high-spatial-resolution zebrafish muscle imaging. Sci Rep 2015;5(1):16625.
22. Larsson DH, Vågberg W, Yaroshenko A, Yildirim AÖ, Hertz HM. High-resolution short-exposure small-animal laboratory x-ray phase-contrast tomography. Sci Rep 2016;6(1):39074.
23. Töpperwien M, Krenkel M, Vincenz D, et al. Three-dimensional mouse brain cytoarchitecture revealed by laboratory-based x-ray phase-contrast tomography. Sci Rep 2017;7(1):42847.
24. Vågberg W, Persson J, Szekely L, Hertz HM. Cellular-resolution 3D virtual histology of human coronary arteries using x-ray phase tomography. Sci Rep 2018;8(1):11014.
25. Preissner M, Murrie RP, Pinar I, et al. High resolution propagation-based imaging system for in vivo dynamic computed tomography of lungs in small animals. Phys Med Biol 2018;63(8):08NT03.
26. Mayo SC, Miller PR, Wilkins SW, et al. Quantitative x-ray projection microscopy: phase-contrast and multi-spectral imaging. J Microsc 2002;207(Pt 2):79–96.
27. Hemberg O, Otendal M, Hertz HM. Liquid-metal-jet anode electron-impact x-ray source. Appl Phys Lett 2003;83(7):1483–1485.
28. Paganin D, Mayo SC, Gureyev TE, Miller PR, Wilkins SW. Simultaneous phase and amplitude extraction from a single defocused image of a homogeneous object. J Microsc 2002;206(Pt 1):33–40.
29. Morcuende JA, Sanders JO. Embryology and development of the neuromuscular apparatus. In: Weinstein SL, Flynn JM, eds. Lovell and Winter's pediatric orthopaedics, Vol 1. Philadelphia, Pa: Lippincott Williams & Wilkins, 2014; 28–30.
30. Ohrström LM, von Waldburg H, Speier P, Bock M, Suri RE, Rühli FJ. Scenes from the past: MR imaging versus CT of ancient Peruvian and Egyptian mummified tissues. RadioGraphics 2013;33(1):291–296.
31. Ohrström L, Bitzer A, Walther M, Rühli FJ. Technical note: terahertz imaging of ancient mummies and bone. Am J Phys Anthropol 2010;142(3):497–500.
32. Putz R, Pabst R. Sobotta Atlas of human anatomy. Vol 1: Head, neck, upper limb. Munich, Germany: Urban & Fischer, 2006.
33. Ross MH, Romrell LJ, Kaye GI. Histology: a text and atlas. Philadelphia, Pa: Lippincott Williams & Wilkins, 1995.
34. Mocella V, Brun E, Ferrero C, Delattre D. Revealing letters in rolled Herculaneum papyri by x-ray phase-contrast imaging. Nat Commun 2015;6(1):5895.
35. Tafforeau P, Boistel R, Boller E, et al. Applications of x-ray synchrotron microtomography for non-destructive 3D studies of paleontological specimens. Appl Phys A Mater Sci Process 2006;83(2):195–202.
36. Müller M, de Sena Oliveira I, Allner S, et al. Myoanatomy of the velvet worm leg revealed by laboratory-based nanofocus X-ray source tomography. Proc Natl Acad Sci U S A 2017;114(47):12378–12383.